

# Super-resolving multi-photon interferences with independent light sources

S. Oppel,<sup>1,2</sup> T. Büttner,<sup>1</sup> P. Kok,<sup>3</sup> and J. von Zanthier<sup>1,2</sup>

<sup>1</sup>*Institut für Optik, Information und Photonik, Universität Erlangen-Nürnberg, 91058 Erlangen, Germany*

<sup>2</sup>*Erlangen Graduate School in Advanced Optical Technologies (SAOT),  
Universität Erlangen-Nürnberg, 91052 Erlangen, Germany*

<sup>3</sup>*Department of Physics and Astronomy, University of Sheffield, Sheffield S3 7RH, United Kingdom*

(Dated: February 13, 2012)

Multi-photon interferences with indistinguishable photons from independent light sources are at the focus of current research owing to their potential in optical quantum computing [1, 2], creating remote entanglement for quantum computation and communication [3, 4] and quantum metrology [5]. The paradigmatic states for multi-photon interference are the highly entangled NOON states [6], which can be used to achieve increased resolution in spectroscopy [7, 8], interferometry [9–12], lithography [6, 13] and microscopy [14]. Multi-photon interferences from independent, uncorrelated emitters can also lead to enhanced resolution in metrology and imaging [13–16]. So far, such interferences have been observed with maximally two independent emitters [13, 17–26]. Here, we report multi-photon interferences with up to five independent emitters, displaying interference patterns equivalent to those of NOON states. Experimental results with independent thermal light sources confirm this NOON-like modulation. The experiment is an extension of the landmark measurement by Hanbury Brown and Twiss who investigated intensity correlations of second order [15]. Here we go beyond this level by measuring spatial intensity correlations up to fifth order to further increase the resolution. The inherent simplicity of our scheme opens up the possibility of improved imaging in astronomy and biology.

Multi-photon interference lies at the heart of optical quantum information processing [27] and is an essential ingredient in optical quantum computing [1, 2], quantum metrology with light [5] and quantum imaging [6, 13, 14, 16]. Multi-photon interference lies also at the heart of the Hanbury Brown and Twiss experiment [15]. One of the key signatures of classical and quantum multi-photon interference is *super-resolution*, that is, the appearance of fringes that are much denser than those obtained with standard interference techniques.

In its simplest form the interference pattern can be described by the relation

$$I_N(\mathbf{x}) \propto \frac{1}{2} [1 + V_N \cos(N \mathbf{k} \cdot \mathbf{x})], \quad (1)$$

where  $N$  is the number of photons participating in the interference,  $V_N$  is the visibility,  $\mathbf{k}$  is the difference between the wave vectors  $\mathbf{k}_1$  and  $\mathbf{k}_2$  of the interfering light fields, with  $|\mathbf{k}_1| = |\mathbf{k}_2| = 2\pi/\lambda$ , and  $\mathbf{x}$  is the position along the interference pattern. When for a given numerical aperture  $\mathcal{A}$  of the image formation system  $N > 1$ , the pattern exhibits super-resolution and conveys information about source details that are smaller than the Abbe limit; when  $N\mathcal{A} > 1$  the interference pattern is sensitive to source structures below  $\lambda$  [28]. This is the fundamental principle behind quantum lithography, where multi-photon interference produces sub-wavelength features [6, 13].

The archetypal quantum state used for demonstrating super-resolution is the so-called NOON state [6]. Imagine a two-photon absorbing substrate that is sensitive to the square of the incoming intensity. If it is exposed to a standing light field of the form  $I \propto \cos^2 \varphi$ , with  $\varphi = \mathbf{k} \cdot \mathbf{x}$ , the absorption rate of the substrate scales with  $I^2 \propto 3 + 4 \cos(2\varphi) + \cos(4\varphi)$ . If one could eliminate the middle term containing the slowly varying function  $\cos(2\varphi)$ , one would be left with an interference pattern displaying a fringe spacing of  $\lambda/4$ , a factor of two improvement with respect to the classical resolution limit [6]. An  $N$ -photon NOON state  $(|N, 0\rangle + e^{iN\varphi}|0, N\rangle)/\sqrt{2}$  is able to achieve this task, because the photons always travel together, effectively behaving like a single particle with a de Broglie wavelength  $\lambda/N$ . When the two modes of a NOON state are made to interfere, super-resolution according to Eq. (1) occurs due to the  $N$ -fold amplified relative phase factor  $\exp(iN\varphi)$ . However, NOON states are extremely difficult to realize and fragile to noise and decoherence; moreover, the measurement procedure requires  $N$ -photon absorbing media. For these reasons NOON states are very hard to use in practice.

Super-resolution can also be obtained with independent photon emitters, even though the photons no longer behave as a single particle with reduced de Broglie wavelength. In this case the slowly varying terms can be removed by exploiting  $N^{\text{th}}$ -order intensity interference effects. For example, for  $N$  independent photon sources and  $N$  detectors at carefully chosen positions  $\mathbf{r}_2, \dots, \mathbf{r}_N$ , the  $N^{\text{th}}$ -order spatial intensity correlation function  $g^{(N)}(\mathbf{r}_1, \dots, \mathbf{r}_N)$  as a function of  $\mathbf{r}_1$  can be shown to exhibit a NOON-like modulation of the form  $\cos[(N-1)\delta_1]$ , with  $\delta_1 = kd \sin \theta_1$  (see Fig. 1) [16, 29]. This approach does not rely on particular states of light

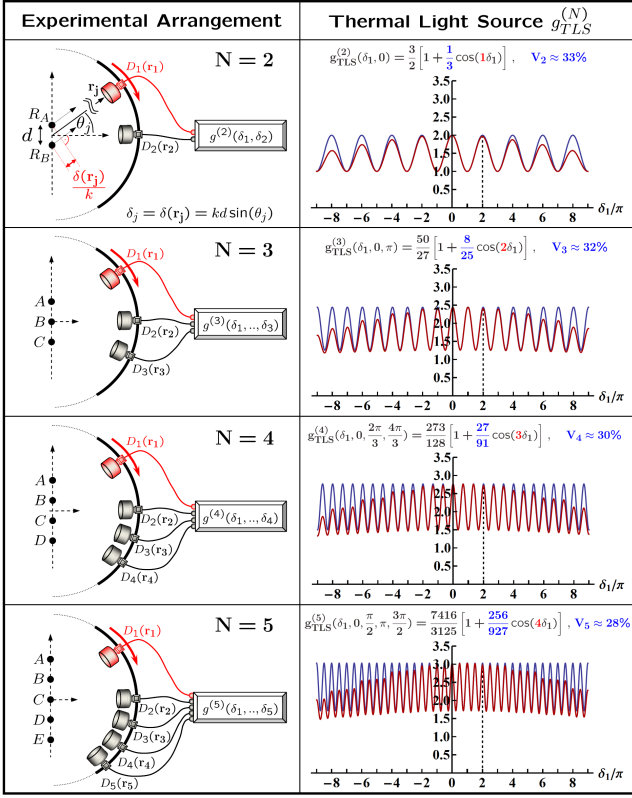


FIG. 1:  $N$ -photon coincidence detection scheme for  $N$  independent SPE or TLS (left) and calculated  $N^{\text{th}}$  order spatial correlation functions for TLS (right). Left column: Detection scheme for the measurement of the normalized  $N^{\text{th}}$  order spatial correlation function  $g^{(N)}(\delta_1, \dots, \delta_N)$  for  $N = 2, \dots, 5$  point-like independent emitters located at  $\mathbf{R}_\alpha$  along a chain with equal spacing  $d$  ( $\alpha = A, B, \dots$ ). An equal number of  $N$  detectors  $D_j$  situated at  $\mathbf{r}_j$  ( $j = 1, \dots, N$ ) measure the  $N$  emitted photons in the far field, so that they cannot distinguish from which of the  $N$  sources the photons originate.  $\delta_j = \delta(\mathbf{r}_j) = kd \sin \theta_j$  is the optical phase difference of two photons propagating from adjacent sources to detector  $D_j$ . A successful  $N$ -photon coincident detection event is defined if all  $N$  detectors register one photon within a joint detection time interval. Right column: Theoretical plots of  $g^{(N)}(\delta_1, \dots, \delta_N)$  for  $N = 2, \dots, 5$  TLS for the indicated fixed detector positions  $\delta_j$  ( $j = 2, \dots, N$ ) as a function of  $\delta_1$  for point-like emitters (blue curve) and extended emitters (red curve).

nor on  $N$ -photon absorbing media, only on  $N$ -fold coincidences in  $N$  separate single photon detectors.

The occurrence of super-resolution can be used to enhance the resolution in imaging and microscopy. According to Abbe, an image of an object is formed if the rays contributing to the first diffraction order in the diffraction plane are captured by the imaging device since then all information about the object is contained in the diffraction pattern via Fourier transform [28]. For a grating with  $N$  slits and slit spacing  $d$  this leads to a minimal resolvable slit separation  $d_{\min} = \lambda/(2\mathcal{A})$ , with an error

of  $\Delta d_{\min} = \lambda/(4\mathcal{A})$ . This limit can be overcome if the slowly oscillating terms in the diffraction pattern of the grating  $I \propto 1 + \frac{2}{N} \sum_{\alpha=1}^{N-1} (N-\alpha) \cos(\alpha\delta)$  are suppressed, such that only the modulation at the highest frequency  $\cos[(N-1)\delta]$  prevails. This modulation already contains all relevant parameters of the grating ( $N$  and  $d$ ). Based on counting the number of peaks  $M$  in the interference pattern  $1 + V_N \cos[(N-1)\delta]$  across  $\mathcal{A}$ , we find that the separation  $d$  and its corresponding error  $\Delta d$  are given by (see supplementary information)

$$d = \frac{M\lambda}{2\mathcal{A}(N-1)} \quad \text{and} \quad \Delta d = \frac{\lambda}{4\mathcal{A}(N-1)}. \quad (2)$$

For  $N-1 > M \geq 1$  the procedure allows to achieve a resolution beyond the Abbe limit. Here, we experimentally demonstrate an increased resolution compared to the canonical classical limit using up to  $N = 5$ .

Consider  $N$  independent light sources at  $\mathbf{R}_\alpha$  ( $\alpha = A, B, \dots$ ) along a chain with equal spacing  $d$ , and place  $N-1$  detectors in a semi-circle in the far field around the sources at specific *magic angles* (see Fig. 1). The sources have identical frequency and polarisation and may be single photon emitters (SPE) or thermal light sources (TLS). Moving another detector along the semi-circle and post-selecting on simultaneous single photon detection events in each of the  $N$  detectors will produce an interference pattern of the form of Eq. (1). The interference pattern is proportional to the (normally ordered)  $N$ -point intensity correlation function

$$g^{(N)}(\mathbf{r}_1, \dots, \mathbf{r}_N) \equiv \frac{\langle : \prod_k \hat{E}^{(-)}(\mathbf{r}_k) \hat{E}^{(+)}(\mathbf{r}_k) : \rangle}{\prod_m \langle \hat{E}^{(-)}(\mathbf{r}_m) \hat{E}^{(+)}(\mathbf{r}_m) \rangle}, \quad (3)$$

where  $\langle \dots \rangle$  denotes the quantum mechanical expectation value and  $\hat{E}^{(+)}(\mathbf{r})$  and  $\hat{E}^{(-)}(\mathbf{r})$  are the positive and negative frequency parts of the total electric field operator at position  $\mathbf{r}$ , respectively. Here,  $\hat{E}^{(+)}(\mathbf{r}_j) \propto \sum_\alpha \hat{a}_\alpha e^{ikr_{\alpha j}}$ , where  $\hat{a}_\alpha$  is the annihilation operator of a photon of source  $\alpha$  and  $r_{\alpha j} = |\mathbf{R}_\alpha - \mathbf{r}_j|$  is the distance between the source  $\alpha$  and the detector  $D_j$ . Since the emitters are independent and uncorrelated, the state of the field is described by  $\rho = \otimes_\alpha \rho_\alpha$ , where  $\rho_\alpha = \sum_n P_\alpha(n) |n\rangle \langle n|$  and  $P_\alpha(n)$  denotes the photon number distribution for the modes originating from source  $\alpha$ . From this, the interference pattern  $g^{(N)}$  is easily calculated (see supplementary information).

The quantum paths that contribute to  $g^{(2)}$  and  $g^{(3)}$  in the case of SPE and TLS are shown in Fig. 2. For  $N$  SPE the number of quantum paths that contribute to the  $N$ -photon signal is  $N!$ , whereas for  $N$  TLS  $N^N$  quantum paths are involved. The increased number of paths in case of TLS is due to the possibility of multiple photons originating from the same TLS, which reduces the visibility of  $g^{(N)}$ .

The form of  $g^{(N)}$  is highly dependent on the positions  $\mathbf{r}_j$  of the  $N$  detectors. We can choose the  $\mathbf{r}_j$  such that,

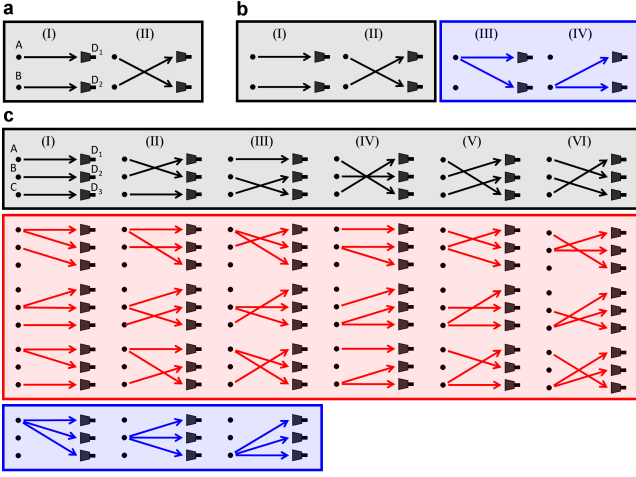


FIG. 2: **Quantum paths contributing to two- and three-photon joint detection events in case of  $N = 2$  and  $N = 3$  emitters, respectively.** Sources  $A$  and  $B$  are (a) two SPE [paths (I) and (II)] or (b) two TLS [paths (I) - (IV)]. In the case of TLS only the two indistinguishable quantum paths (I) and (II) contribute to the interference signal whereas paths (III) and (IV) lead to a constant offset and thus a reduced visibility. (c) Sources  $A$ ,  $B$  and  $C$  are three SPE or TLS. In case of SPE  $3! = 6$  quantum paths contribute to  $g^{(N)}$  [first row, paths (I)-(VI)], whereas for TLS  $3^3 = 27$  quantum paths are involved, since in this case more than one photon may originate from the same source. All quantum paths where the same number of photons is emitted by each source are indistinguishable so that the corresponding quantum paths interfere coherently. The different colours refer to the case where one photon originates from each source (grey), all  $N$  photons originate from the same source (blue) or two photons originate from one source (red). The six indistinguishable quantum paths in the first row in (c) are identical for SPE and TLS.

up to a proportionality constant,  $g^{(N)}$  takes the form of  $I_{N-1}$  in Eq. (1), where one detector is moved and  $N - 1$  detectors are kept at the fixed magic positions. In this case, for SPE, the second order correlation function in terms of phases  $\delta_j = kd \sin \theta_j$  can be written in the form

$$g_{SPE}^{(2)}(\delta_1, \delta_2 = 0) = \frac{1}{2} [1 + \cos(\delta_1)] , \quad (4)$$

while the third order correlation function becomes

$$g_{SPE}^{(3)}\left(\delta_1, \delta_2 = \frac{\pi}{4}, \delta_3 = \frac{7\pi}{4}\right) = \frac{4}{27} [1 + \cos(2\delta_1)] . \quad (5)$$

From Eqs. (4) and (5) one can see that for SPE the visibility of the second and third order correlation function is 100%; this remains true for any order  $N$ . In the same way, the second and third order correlation function for TLS with the detectors at the magic positions are

$$g_{TLS}^{(2)}(\delta_1, 0) = \frac{3}{2} \left[ 1 + \frac{1}{3} \cos(\delta_1) \right] \quad (6)$$

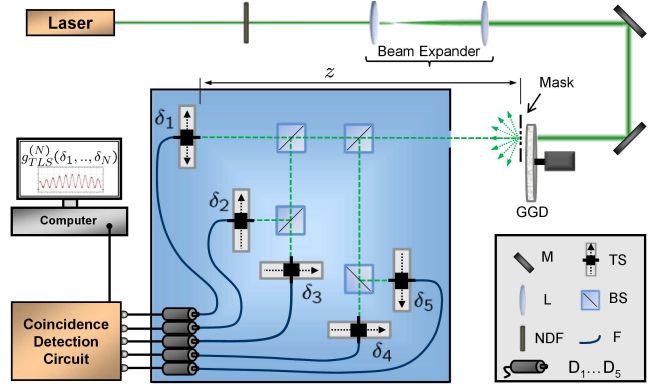


FIG. 3: **Experimental setup for the multi-photon interference measurement.** The  $N = 2, \dots, 5$  independent TLS are realized by opaque masks with  $N$  slits of width  $a = 25 \mu\text{m}$  and separation  $d = 250 \mu\text{m}$ , illuminated by pseudo-thermal light using a linearly polarized Nd:YAG laser at  $\lambda = 532 \text{ nm}$  and a rotating ground glass disc. The coherence time of the pseudo-thermal light source was chosen to  $\tau_c \approx 100 \mu\text{s}$ . The light from the masks is separated by 50/50 non-polarizing beam splitters into  $N$  beams. To measure  $g_{TLS}^{(N)}(\delta_1, \dots, \delta_N)$ ,  $N$  laterally displaceable fibre tips with  $50 \mu\text{m}$  core diameter are located  $z \approx 1 \text{ m}$  away from the masks, mounted on translation stages, which collect the photons and guide them to single photon detectors. The output pulses of the  $N$  single photon detectors are fed into a coincidence detection circuit. GGD: ground glass disc, M: mirror, L: lens, NDF: neutral density filter, TS: translation stage with fibre mount, BS: beam splitter, F: multimode fibre,  $D_1 \dots D_5$ : photomultiplier modules.

and

$$g_{TLS}^{(3)}(\delta_1, 0, \pi) = \frac{50}{27} \left[ 1 + \frac{8}{25} \cos(2\delta_1) \right] , \quad (7)$$

displaying reduced visibilities  $V_2 = 1/3$  and  $V_3 = 8/25$ , respectively. In all cases the super-resolving NOON-like modulation of  $g^{(N)}(\delta_1)$  is clearly visible.

Similar results are obtained for higher numbers of SPE and TLS. In the case of TLS, the interference pattern  $g_{TLS}^{(N)}$  always reduces to the form  $I_{N-1}$  in Eq. (1) when the detector positions are chosen as  $\delta_j = 2\pi(j-2)/(N-1)$  for  $j = 2, \dots, N$ . The calculated interference signals  $g_{TLS}^{(N)}(\delta_1)$  for  $N = 2, \dots, 5$  independent TLS are displayed in Fig. 1, together with their exact analytical expressions.

The experimental setup used to measure  $g_{TLS}^{(N)}(\delta_1)$  is shown in Fig. 3. To realize the  $N$  independent TLS, opaque masks with  $N$  identical slits are illuminated by pseudo-thermal light originating from a laser scattered by a rotating ground glass disc [30]. The large number of time-dependent speckles, produced by the stochastically interfering waves scattered from the granular surface of the disc, act within a given slit as many independent point-like sub-sources equivalent to an ordinary spatial incoherent thermal source. The coherence time of the pseudo-thermal light sources depends on the rotational



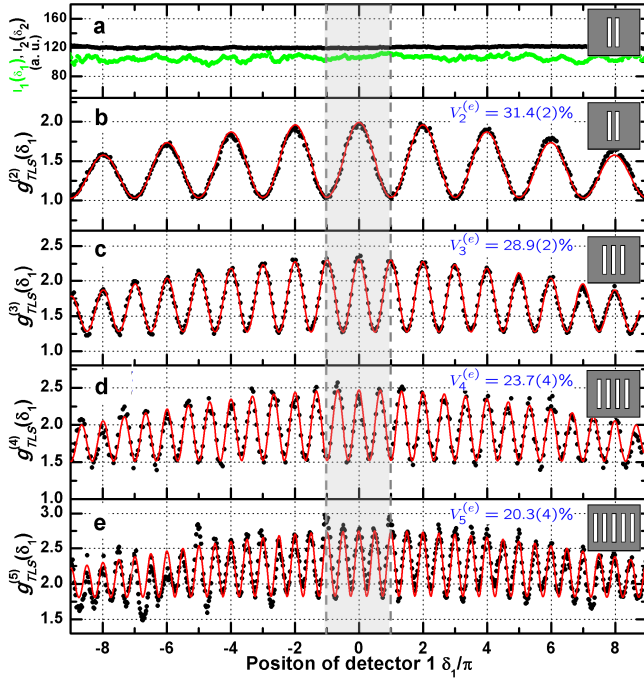


FIG. 4: **Experimental results.** (a) Measurement of average intensities  $I_1$  and  $I_2$  at detectors  $D_1$  and  $D_2$  with  $D_1$  scanned and  $D_2$  kept constant. Since the pseudo-thermal light sources are spatially incoherent in first order no first-order interference pattern is observed. (b)-(e) Measurement of the normalized  $N^{\text{th}}$  order spatial correlation function  $g_{TLS}^{(N)}$  as a function of  $\delta_1$  in case of  $N = 2, \dots, 5$  TLS for particular detector positions  $\delta_2, \dots, \delta_N$ . Red curves correspond to a theoretical fit taking into account the finite width of the slits. The only fitting parameters are the slit separation  $d$ , the slit width  $a$  and the visibility  $V_N^{(e)}$ . The experimentally obtained visibilities  $V_N^{(e)}$  can be compared with the theoretical values  $V_N$  in Fig. 1. Single photon counting rates for  $g_{TLS}^{(2)}$ ,  $g_{TLS}^{(3)}$ ,  $g_{TLS}^{(4)}$  and  $g_{TLS}^{(5)}$  are about 200 kHz which with joint detection time windows of 50 ns, 410 ns, 410 ns and 850 ns lead to averaged  $N$ -fold coincidence rates of 1500 Hz, 1500 Hz, 400 Hz and 300 Hz, respectively.

speed of the disk and can be, for example, of the order of microseconds. Note that  $g_{TLS}^{(N)}(\delta_1)$  displays the calculated interference signal only if the  $N$  photons are registered within their coherence time [15].

The experimental results for  $g_{TLS}^{(2)}(\delta_1)$  to  $g_{TLS}^{(5)}(\delta_1)$  are shown in Fig. 4. From the figure it can be seen that the measured curves for  $g_{TLS}^{(3)}(\delta_1)$ ,  $g_{TLS}^{(4)}(\delta_1)$  and  $g_{TLS}^{(5)}(\delta_1)$  display a doubled ( $2\delta_1$ ), tripled ( $3\delta_1$ ) and quadrupled ( $4\delta_1$ ) modulation frequency compared to  $g_{SPE}^{(2)}(\delta_1, 0)$  and  $g_{TLS}^{(2)}(\delta_1, 0)$  [see Eqs. (4) and (6)]. Due to the offset appearing for TLS the visibilities  $V_N$  of  $g_{TLS}^{(N)}(\delta_1)$  are slowly decreasing with  $N$  whereas for SPE the visibilities always remain 100%. Fig. 4 (a) exhibits the average intensities at detectors  $D_1$  and  $D_2$  for a typical measurement of  $g_{TLS}^{(N)}$ , demonstrating that the pseudo-thermal light used is indeed spatially incoherent in first order of the intensity.

The measured curves for  $g_{TLS}^{(2)}(\delta_1)$  to  $g_{TLS}^{(5)}(\delta_1)$  are in excellent agreement with the theoretical prediction if one takes into account the finite width of the slits [see red solid lines in Fig. 1 and Fig. 4 (b)-(e)]. The theoretically predicted and experimentally observed visibilities,  $V_N$  and  $V_N^{(e)}$ , are listed in Fig. 1 and Fig. 4 (b)-(e), respectively. The differences between  $V_N^{(e)}$  and  $V_N$  towards higher  $N$  are mainly due to increased dead time effects arising from larger joint detection time windows and higher single photon counting rates at the  $N$  detectors. The small deviations between the experimental results and the theoretical curves for  $g_{TLS}^{(4)}$  and  $g_{TLS}^{(5)}$  are mostly due to a slight misalignment of the detector positions from the required magic values. From Fig. 4 it can be seen that for a given aperture  $\mathcal{A}$  (grey bar in Fig. 4)  $g_{TLS}^{(5)}(\delta_1)$  exhibits four times more oscillations than  $g_{TLS}^{(2)}(\delta_1)$ , which corresponds to an enhancement in  $\Delta d$  by a factor of four, and can be used to beat the Abbe limit.

In conclusion, we have demonstrated spatial multi-photon interference patterns displaying super-resolution with up to five independent emitters, using pseudo-thermal light sources. For  $N > 2$ , these experiments achieve a higher resolution than the canonical classical limit for imaging the spatial structure of the light source. In case of  $N$  SPE, the independent sources produce an interference pattern identical to the one of NOON states with  $N - 1$  photons. The same is true for  $N$  TLS, except for a reduced visibility. Our technique does not require special quantum tailoring of light nor  $N$ -photon absorbing media; it relies only on single photon detectors. The natural low light requirements suggest that the technique has potential applications for improved imaging of faint star clusters and in vivo biological samples.

### Supplementary information:

First, we derive Eq. (2) in the paper. According to Abbe, an image of an object can only be formed if the rays contributing to the first diffraction order in the diffraction plane are captured by the imaging device [28]. In case of a grating with  $N$  slits and slit spacing  $d$  this leads to a minimal resolvable slit separation and error [28]

$$d_{\min} = \frac{\lambda}{2\mathcal{A}} \quad \text{and} \quad \Delta d_{\min} = \frac{\lambda}{4\mathcal{A}}, \quad (8)$$

where  $\mathcal{A}$  is the numerical aperture of the imaging device and  $\lambda$  the wavelength. In case of  $\mathcal{A} = 1$  we obtain  $d_{\min} = \lambda/2$ . This limit can be overcome if the slowly varying terms in the diffraction pattern of the grating

$$I(\mathbf{r}) \propto 1 + \frac{2}{N} \sum_{\alpha=1}^{N-1} (N - \alpha) \cos(\alpha\delta), \quad (9)$$

with  $\delta = \delta(\mathbf{r}) = kd \sin \theta$ , are dispelled so that only the modulation at the highest oscillation frequency

$\cos[(N-1)\delta]$  prevails. For a given  $\mathcal{A}$ , this allows to determine a slit separation as low as  $d_{\min} = \lambda/2\mathcal{A}(N-1)$  with an uncertainty of  $\Delta d_{\min} = \lambda/4\mathcal{A}(N-1)$ . This can be seen from the following argument: let the modulation  $\cos[(N-1)\delta]$  display  $M$  peaks over the range of the numerical aperture ( $-\mathcal{A} \leq \sin\theta \leq \mathcal{A}$ ), such that

$$2\pi M = 2\mathcal{A}(N-1)kd \implies d = \frac{M\lambda}{2\mathcal{A}(N-1)} \quad (10)$$

with  $k = 2\pi/\lambda$ . The uncertainty in  $d$  can be estimated conservatively by choosing  $\Delta M = 1/2$ , what leads to

$$\Delta d_{\min} = \Delta M \left| \frac{\partial M}{\partial d} \right|^{-1} = \frac{\lambda}{4\mathcal{A}(N-1)}. \quad (11)$$

For  $N-1 > M \geq 1$  we can thus surpass the canonical classical limit given in Eq. (8). Counting only a single peak ( $M = 1$ ) we obtain

$$d_{\min} = \frac{\lambda}{2\mathcal{A}(N-1)}, \quad (12)$$

which is the new minimum resolvable slit separation. In case of  $\mathcal{A} = 1$  we obtain  $d_{\min} = \lambda/2(N-1)$ .

Next, we calculate the analytical expressions for  $G^{(1)}$ ,  $g^{(2)}$  and  $g^{(3)}$ . For  $N = 2$  we have  $\rho = \rho_A \otimes \rho_B$  with  $\rho_\alpha = \sum_n P_\alpha(n)|n\rangle\langle n|$ ,  $\alpha = A, B$ , and  $\hat{E}^{(+)}(\mathbf{r}_j) = \hat{A}_j^{(+)} + \hat{B}_j^{(+)} \propto \hat{a}_A e^{ikr_{Aj}} + \hat{a}_B e^{ikr_{Bj}}$ . With this we find from Eq. (3) in the paper that the intensity distribution  $G^{(1)}(\mathbf{r}_1)$  at the detector  $D_1$  is given by

$$\begin{aligned} G^{(1)}(\mathbf{r}_1) &= \sum_{n,m=0}^{\infty} P_A(n)P_B(m) \left[ |\langle n-1, m | \hat{A}_1^{(+)} | n, m \rangle|^2 \right. \\ &\quad \left. + |\langle n, m-1 | \hat{B}_1^{(+)} | n, m \rangle|^2 \right] \\ &\propto \langle n_A \rangle + \langle n_B \rangle = 2\langle n \rangle = \text{const}, \end{aligned} \quad (13)$$

where in the last equation we assumed equal amplitudes, that is, equal mean photon numbers  $\langle n \rangle = \langle n_\alpha \rangle = \langle \hat{a}_\alpha^\dagger \hat{a}_\alpha \rangle$  in the modes from source  $\alpha$ . Eq. (13) shows that irrespective of the distribution  $P_\alpha(n)$ , no interference in the first order spatial intensity correlation function can be seen. This is due to the fact that the two sources are uncorrelated.

Now, we derive  $g^{(2)}(\mathbf{r}_1, \mathbf{r}_2)$ . Using the result of Eq. (13) we find

$$\begin{aligned} g^{(2)}(\mathbf{r}_1, \mathbf{r}_2) &= \frac{1}{(\langle n_A \rangle + \langle n_B \rangle)^2} \sum_{n,m=0}^{\infty} P_A(n)P_B(m) \left[ |\langle n-1, m-1 | (\hat{A}_2^{(+)} \hat{B}_1^{(+)} + \hat{B}_2^{(+)} \hat{A}_1^{(+)}) | n, m \rangle|^2 \right. \\ &\quad \left. + |\langle n-2, m | \hat{A}_2^{(+)} \hat{A}_1^{(+)} | n, m \rangle|^2 + |\langle n, m-2 | \hat{B}_2^{(+)} \hat{B}_1^{(+)} | n, m \rangle|^2 \right]. \end{aligned} \quad (14)$$

In the case where  $A$  and  $B$  correspond to single photon emitters (SPE) we have  $P_\alpha(1) = 1$  and  $P_\alpha(n \neq 1) = 0$ , so that only the first term in Eq. (14) contributes to  $g^{(2)}(\mathbf{r}_1, \mathbf{r}_2)$ . We thus obtain

$$\begin{aligned} g_{SPE}^{(2)}(\mathbf{r}_1, \mathbf{r}_2) &= \frac{1}{4} |e^{ik(r_{A1} + r_{B2})} + e^{ik(r_{B1} + r_{A2})}|^2 \\ &= \frac{1}{2} [1 + \cos(\delta_2 - \delta_1)], \end{aligned} \quad (15)$$

where  $\delta_j = \delta(\mathbf{r}_j) = k(r_{Aj} - r_{Bj})$  is the relative phase illustrated in Fig. 1. Thus, even though the two SPE emit their photons independently and no information is contained in  $G^{(1)}(\mathbf{r}_1)$ , the normalized second order spatial intensity correlation function  $g_{SPE}^{(2)}(\delta_1, \delta_2)$  displays a sinusoidal modulation with a visibility of 100% and may convey information about the spatial distribution of the sources.

In the case where  $A$  and  $B$  correspond to thermal light sources (TLS), the probability distribution  $P_\alpha(n)$  is given

by Bose-Einstein statistics

$$P_\alpha(n) = \frac{\langle n_\alpha \rangle^n}{(1 + \langle n_\alpha \rangle)^{n+1}}. \quad (16)$$

In this case, the terms in Eq. (14) where more than one photon originate from the same source do not vanish. The initial state  $|n, m\rangle$  can thus lead to  $\binom{2N-1}{N} = 3$  different final states, namely  $\langle n-1, m-1|$ ,  $\langle n-2, m|$  and  $\langle n, m-2|$ . Here, different quantum paths linking the same initial and final state are indistinguishable and therefore have to be added coherently, whereas quantum paths leading to different final states, being distinguishable, have to be summed incoherently. From the  $N^N = 4$  two-photon probability amplitudes appearing in Eq. (14) [represented by the quantum paths (I)-(IV) in Fig. 2(b)], only paths (I) and (II) give rise to interference whereas paths (III) and (IV) contribute to the offset of the two-photon signal. Summing the contributions for the different states  $|n, m\rangle$ , assuming equal mean photon numbers in each mode and taking into account the Bose-Einstein

statistics of thermal light sources  $P_\alpha(n)$ , we arrive at

$$g_{TLS}^{(2)}(\delta_1, \delta_2) = \frac{3}{2} \left[ 1 + \frac{1}{3} \cos(\delta_2 - \delta_1) \right]. \quad (17)$$

Comparing Eq. (17) with Eq. (15), one can see that the same sinusoidal modulation is obtained for two TLS as for

two SPE, the additional terms in Eq. (17) only reducing the visibility of the two-photon signal from 100% to 33%.

For  $N = 3$  emitters,  $\hat{E}^{(+)}(\mathbf{r}_j)$  is given by the superposition of three fields  $\hat{E}^{(+)}(\mathbf{r}_j) = \hat{A}_j^{(+)} + \hat{B}_j^{(+)} + \hat{C}_j^{(+)} \propto \hat{a}_A e^{ikr_{Aj}} + \hat{a}_B e^{ikr_{Bj}} + \hat{a}_C e^{ikr_{Cj}}$ . In this case  $g^{(3)}(\mathbf{r}_1, \mathbf{r}_2, \mathbf{r}_3)$  calculates to

$$\begin{aligned} g^{(3)}(\mathbf{r}_1, \mathbf{r}_2, \mathbf{r}_3) = & \frac{1}{(\langle n_A \rangle + \langle n_B \rangle + \langle n_C \rangle)^3} \sum_{k,n,m} P(k)P(n)P(m) \left[ \right. \\ & \left| \langle k-1, n-1, m-1 | \left( \hat{A}_3^{(+)} \hat{B}_2^{(+)} \hat{C}_1^{(+)} + \hat{B}_3^{(+)} \hat{A}_2^{(+)} \hat{C}_1^{(+)} + \dots + \hat{C}_3^{(+)} \hat{B}_2^{(+)} \hat{A}_1^{(+)} \right) | k, n, m \rangle \right|^2 \\ & + \left| \langle k-2, n-1, m | \left( \hat{A}_3^{(+)} \hat{A}_2^{(+)} \hat{B}_1^{(+)} + \hat{A}_3^{(+)} \hat{B}_2^{(+)} \hat{A}_1^{(+)} + \hat{B}_3^{(+)} \hat{A}_2^{(+)} \hat{A}_1^{(+)} \right) | k, n, m \rangle \right|^2 + \dots \\ & \left. + \left| \langle k-3, n, m | \hat{A}_3^{(+)} \hat{A}_2^{(+)} \hat{A}_1^{(+)} | k, n, m \rangle \right|^2 + \dots \right]. \end{aligned} \quad (18)$$

When  $A$ ,  $B$  and  $C$  represent SPE, the correlation function reduces to

$$\begin{aligned} g_{SPE}^{(3)}(\mathbf{r}_1, \mathbf{r}_2, \mathbf{r}_3) = & \frac{1}{27} \left| e^{ik(r_{A1}+r_{B2}+r_{C3})} + e^{ik(r_{A2}+r_{B1}+r_{C3})} \right. \\ & + e^{ik(r_{A1}+r_{B3}+r_{C2})} + e^{ik(r_{A3}+r_{B2}+r_{C1})} \\ & \left. + e^{ik(r_{A3}+r_{B1}+r_{C2})} + e^{ik(r_{A2}+r_{B3}+r_{C1})} \right|^2. \end{aligned} \quad (19)$$

The corresponding quantum paths are shown in the first row of Fig. 2(c). If one places the second and third detector at positions such that  $\delta_2 = \pi/4$  and  $\delta_3 = 7\pi/4$ , we obtain from Eq. (19)

$$g_{SPE}^{(3)}\left(\delta_1, \frac{\pi}{4}, \frac{7\pi}{4}\right) = \frac{4}{27} [1 + \cos(2\delta_1)], \quad (20)$$

that is, a sinusoidal modulation which, apart from a scaling factor, oscillates at two times the frequency obtained for  $g_{SPE}^{(2)}(\delta_1, 0)$  [see Eq. (15)]. This is identical to the modulation of a NOON state with  $N = 2$ .

When the sources  $A$ ,  $B$  and  $C$  represent TLS, again terms where two or more photons originate from the same source do not vanish. The initial state  $|k, n, m\rangle$  may thus end up in  $\binom{2N-1}{N} = 10$  different final states, leading to a total of  $N^N = 27$  different quantum paths. The corresponding three-photon transition amplitudes are shown in Fig. 2(c). Note that the six quantum paths listed in the first row in Fig. 2(c) are identical to those obtained for three SPE. Summing up the contributions of all possible quantum paths weighted with the corresponding Bose-Einstein photon statistics one obtains  $g_{TLS}^{(3)}(\delta_1, \delta_2, \delta_3)$ . Similar to the case of three SPE, it is also possible in case

of three TLS to reduce  $g_{TLS}^{(3)}(\delta_1, \delta_2, \delta_3)$  to a single sinusoidal modulation with twice the frequency of  $g_{SPE}^{(2)}(\delta_1, 0)$  or  $g_{TLS}^{(2)}(\delta_1, 0)$  by appropriately positioning detectors  $D_2$  and  $D_3$ . For example, if we place  $D_2$  and  $D_3$  at positions  $\mathbf{r}_2$  and  $\mathbf{r}_3$  such that  $\delta_2 = 0$ ,  $\delta_3 = \pi$ , we derive from Eq. (18), assuming again equal mean photon numbers for all three sources

$$g_{TLS}^{(3)}(\delta_1, 0, \pi) = \frac{50}{27} \left[ 1 + \frac{8}{25} \cos(2\delta_1) \right]. \quad (21)$$

Similar results are obtained for higher numbers of SPE or TLS. In the case of TLS, when positioning the detectors such that

$$\delta_j = 2\pi(j-2)/(N-1) \quad \text{for } j = 2, \dots, N, \quad (22)$$

the interference pattern  $g_{TLS}^{(N)}$  always reduces to a NOON-like modulation of the form

$$g_{TLS}^{(N)}(\delta_1) \propto 1 + V_N \cos[(N-1)\delta_1]. \quad (23)$$

Note that the simple relation for the phase shifts Eq. (22) also allows to determine  $N$  if the number of sources is unknown: according to Eq. (22) the pure sinusoidal oscillation Eq. (23) is obtained if the  $N-1$  fixed detectors  $D_2, \dots, D_N$  are separated by equal amounts  $2\pi/(N-1)$  of their phases  $\delta_2, \dots, \delta_N$ . Thus, by enlarging for different numbers of detectors  $N = 2, \dots$  the angles  $\theta_2, \dots, \theta_N$  of detectors  $D_2, \dots, D_N$  in a uniform manner such that the phase relation Eq. (22) is continuously fulfilled, one can monitor the interference pattern  $g_{TLS}^N(\delta_1)$  until the pure sinusoidal modulation is obtained. The emergence of the pure sinusoidal modulation for  $g_{TLS}^N(\delta_1)$  then fixes  $\theta_j$ ,  $j = 2, \dots, N$ , what allows to determine the source distance  $d$  via  $\delta_j = kd \sin \theta_j$ .

Finally, we note that the suppression of redundant data in order to cut out relevant spatial structural information as in Eq. (23) is the goal in various schemes for super resolution in microscopy, either using techniques from classical physics (see, e.g., [31–35]) or from quantum physics (see, e.g., [13, 14, 36–39]). However, our method differs from these schemes as we exploit higher order ( $N > 2$ ) non-local multi-photon interference effects, i.e., interference of non-local  $N$ -photon probability amplitudes where the  $N$  photons appear at all  $N$  detectors at once.

- 
- [1] Knill, E., Laflamme, R. & Milburn, G. J. A scheme for efficient quantum computation with linear optics. *Nature* **409**, 46-52 (2001).
  - [2] O’Brien, J. L., Pryde, G. J., White, A. G., Ralph, T. C. & Branning D. Demonstration of an all-optical quantum controlled-NOT gate. *Nature* **426**, 264-267 (2003).
  - [3] Moehring, D. L. *et al.* Entanglement of single-atom quantum bits at a distance. *Nature* **449**, 68-71 (2007).
  - [4] Olmschenk, S. *et al.* Quantum Teleportation Between Distant Matter Qubits. *Science* **323**, 486-489 (2009).
  - [5] Giovannetti, V., Lloyd, S. & Maccone L. Advances in quantum metrology. *Nature Photonics* **5**, 222-229 (2011).
  - [6] Boto, A. N. *et al.* Quantum Interferometric Optical Lithography: Exploiting Entanglement to Beat the Diffraction Limit. *Phys. Rev. Lett.* **85**, 2733-2736 (2000).
  - [7] Bollinger, J. J., Itano, W. M., Wineland, D. J. & Heinzen, D. J. Optimal frequency measurements with maximally correlated states. *Phys. Rev. A* **54**, R4649-R4652 (1996).
  - [8] Leibfried, D. *et al.* Toward Heisenberg-Limited Spectroscopy with Multiparticle Entangled States. *Science* **304**, 1476-1478 (2004).
  - [9] Yurke, B. Input States for Enhancement of Fermion Interferometer Sensitivity. *Phys. Rev. Lett.* **56**, 1515-1517 (1986).
  - [10] Walther, P. *et al.* De Broglie wavelength of a non-local four-photon state. *Nature* **429**, 158-161 (2004).
  - [11] Mitchell, M. W., Lunde, J. S. & Steinberg, A. M. Super-resolving phase measurements with a multiphoton entangled state. *Nature* **429**, 161-164 (2004).
  - [12] Resch, K. J. *et al.* Time-Reversal and Super-Resolving Phase Measurements. *Phys. Rev. Lett.* **98**, 223601 (2007).
  - [13] D’Angelo, M., Chekhova, M. V. & Shih, Y. Two-photon diffraction and quantum lithography. *Phys. Rev. Lett.* **87**, 013602 (2001).
  - [14] Muthukrishnan, A., Scully, M. O. & Zubairy, M. S. Quantum microscopy using photon correlations. *J. Optics B: Quantum Semiclass. Opt.* **6**, S575-S582 (2004).
  - [15] Hanbury Brown, R., & Twiss, R. Q., Correlation between photons in two coherent beams of light. *Nature* **177**, 27-29 (1956).
  - [16] Thiel, C. *et al.* Quantum Imaging with Incoherent Photons. *Phys. Rev. Lett.* **99**, 133603 (2007).
  - [17] Kaltenbaek, R., Blauensteiner, B., Żukowski, M., Aspelmeyer, M. & Zeilinger, A. Experimental Interference of Independent Photons. *Phys. Rev. Lett.* **96**, 240502 (2006).
  - [18] Beugnon, J. *et al.* Quantum interference between two single photons emitted by independently trapped atoms. *Nature* **440**, 779-782 (2006).
  - [19] Maunz, P. *et al.* Quantum interference of photon pairs from two remote trapped atomic ions. *Nature Phys.* **3**, 538-541 (2007).
  - [20] Gerber, S., *et al.* Quantum interference from remotely trapped ions. *New J. Phys.* **11**, 013032 (2009).
  - [21] Lettow, R. *et al.* Quantum Interference of Tunably Indistinguishable Photons from Remote Organic Molecules. *Phys. Rev. Lett.* **104**, 123605 (2010).
  - [22] Sanaka, K., Pawlis, A., Ladd, T. D., Lischka, K. & Yamamoto, Y. Indistinguishable Photons from Independent Semiconductor Nanostructures. *Phys. Rev. Lett.* **103**, 053601 (2009).
  - [23] Flagg, E. B. *et al.* Interference of Single Photons from Two Separate Semiconductor Quantum Dots. *Phys. Rev. Lett.* **104**, 137401 (2010).
  - [24] Agafonov, I. N., Chekhova, M. V., Iskhakov, T. Sh. & Penin, A. N. High-visibility multiphoton interference of Hanbury Brown–Twiss type for classical light. *Phys. Rev. A* **77**, 053801 (2008).
  - [25] Agafonov, I. N., Chekhova, M. V., Iskhakov, T. Sh. & Wu, L.-A. High-visibility intensity interference and ghost imaging with pseudo-thermal light. *J. Mod. Opt.* **56**, 422-431 (2009).
  - [26] Zhou, Y., Simon, J., Liu, J. & Shih, Y. Third-order correlation function and ghost imaging of chaotic thermal light in the photon counting regime. *Phys. Rev. A* **81**, 043831 (2010).
  - [27] Kok P. & Lovett, B. W. *Introduction to Optical Quantum Information Processing* (Cambridge University Press 2010).
  - [28] Born, M. & Wolf, E. *Principle of Optics* (Cambridge University Press 1998).
  - [29] Agarwal, G. S., von Zanthier, J., Skornia, C. & Walther, H. Intensity-intensity correlations as a probe of interferences under conditions of noninterference in the intensity. *Phys. Rev. A* **65**, 053826 (2002).
  - [30] Rousseau, M. Statistical Properties of Optical Fields Scattered by Random Media. Application of Rotating Ground Glass. *J. Opt. Soc. Am.* **61**, 1307-1316, 1307 (1971).
  - [31] Hell, S. W. & Wichmann, J. Breaking the diffraction resolution limit by stimulated emission: stimulated-emission-depletion fluorescence microscopy. *Opt. Lett.* **19**, 780-782 (1994).
  - [32] Klar, T. A. & Hell, S. W. Subdiffraction resolution in far-field fluorescence microscopy. *Opt. Lett.* **24**, 954-956 (1999).
  - [33] Betzig, E. *et al.* Imaging Intracellular Fluorescent Proteins at Nanometer Resolution. *Science* **313**, 1642-1645 (2006).
  - [34] Hess, S. T., Girirajan, T. P. K. & Mason, M. D. Ultra-High Resolution Imaging by Fluorescence Photoactivation Localization Microscopy. *Biophysical Journal* **91**, 4258-4272 (2006).
  - [35] Rust, M. J., Bates, M. & Zhuang, X. Sub-diffraction-limit imaging by stochastic optical reconstruction microscopy (STORM). *Nature Methods* **3**, 793-796 (2006).
  - [36] Wang, K. & Cao, D.-Z. Subwavelength coincidence interference with classical thermal light. *Phys. Rev. A* **70**, 041801(R) (2004).
  - [37] Zhang, M. *et al.* Sub-wavelength Fourier-transform imaging of a pure-phase object with thermal light. *Phys. Lett. A* **366**, 569-574 (2007).

- [38] Giavonnetti, V., Lloyd, S., Maccone, L. & Shapiro, J. H. Sub-Rayleigh-diffraction-bound quantum imaging. *Phys. Rev. A* **79**, 013827 (2009).
- [39] Guerrieri, F. *et al.* Sub-Rayleigh imaging via N-photon detection. *Phys. Rev. Lett.* **105**, 163602 (2010).